Supplementary for the Paper: Multiphasic Transport in the Human Cranial Dura: How Meningeal Lymphatic Vessels Drive Waste Clearance from Brain Cerebrospinal Fluid

Alberto Girelli[1*], Andreas Solheim[1,6], Kaja Nordengen[2,3], Tryggve Holck Storås[3,4,7], Sofie Lysholm Lian[5], Kent-Andre Mardal[1,6,7]

[1]Department of Numerical Analysis and Scientific Computing, Simula Research Laboratory, Norway.
[2]Department of Neurology, Akershus University Hospital, Lørenskog, Lørenskog, Norway.
[3]Institute of Clinical Medicine, University of Oslo, Oslo, Norway.
[4]Department of Physics and Computational Radiology, Division of Radiology and Nuclear Medicine, Oslo University Hospital, Oslo, Norway.
[5]Oslo University Hospital, Oslo, Norway.
[6]Department of Mathematics, University of Oslo, Moltke Moes vei 35, Oslo, 0851, Norway.
[7] K.G. Jebsen Centre for Brain Fluid Research, University of Oslo, Pb 1072 Blindern, Oslo, 0316, Norway.

*Corresponding author(s). E-mail(s): alberto@simula.no;
Contributing authors: solheim@simula.no; kaja.nordengen@gmail.com; tstoras@uio.no; Sofie.lysholm.lian@gmail.com; kent-and@simula.no;

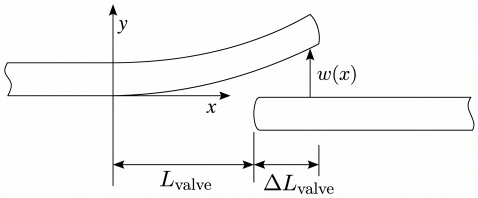

Fig. A: Schematic representation of the lymphatic valve [1]

A mLV Valve Model

We use the model of [1] to obtain an explicit solution of the valve opening of initial lymphatics and consequently estimate the flow passing through this valve. The single primary lymphatic valve is formed by an overlapping endothelial flap of length L_{valve} (free portion) (see Figure A). The flap behaves as an Euler–Bernoulli beam clamped at $x = 0$ and free at $x = L_{\text{valve}} + \Delta L_{\text{valve}}$. We assume a constant trans-wall pressure difference Δp to obtain the explicit solution.

The beam equation is

$$EI\, w''''(x) = \Delta p, \tag{1}$$

with boundary conditions

$$w(0) = 0, \quad w'(0) = 0, \qquad w''(L_{\text{valve}}+\Delta L_{\text{valve}}) = 0, \quad w'''(L_{\text{valve}}+\Delta L_{\text{valve}}) = 0. \tag{2}$$

Solving

$$w(x) = \frac{\Delta p}{24\,EI}\, x^2\big(x^2 - 4(L_{\text{valve}}+\Delta L_{\text{valve}})x + 6(L_{\text{valve}}+\Delta L_{\text{valve}})^2\big), \qquad 0 \le x \le L_{\text{valve}}+\Delta L_{\text{valve}}. \tag{3}$$

We consider steady, incompressible flow between two plates separated by the height $w(x)$. Let μ be the dynamic viscosity, T the valve depth, and Q the volumetric flow rate.

The lubrication equation is

$$\frac{dp}{dx} = -\frac{12\mu q}{w(x)^3} = -\frac{12\mu Q}{T\, w(x)^3}. \tag{4}$$

If we assume a constant pressure gradient, it follows that

$$Q = \frac{\Delta P w^3(x) T}{12 L_{\text{valve}} \mu}, \tag{5}$$

taking the average over x, we have:

$$\bar{Q} = \frac{\Delta P T}{12 L_{\text{valve}}^2 \mu} \int_0^{L+\Delta L} w^3(x) dx \equiv Q_{\text{valve}}. \tag{6}$$

From [2], the permeability relation can be written as

$$L_p = \frac{Q_{\text{prod}}}{S_{\text{mLV}}\, \Delta p}. \tag{7}$$

At the *microscale*, we apply (7) to a single primary lymphatic valve:

$$L_{p,\text{micro}} = \frac{Q_{\text{valve}}}{S_{\text{valve}}\, \Delta p}, \tag{8}$$

where S_{valve} is the local valve surface area.

Then we have that the estimated number of valves can be computed by

$$N_{\text{valve}} = \frac{Q_{\text{prod}}}{Q_{\text{valve}}}. \tag{9}$$

It follows that we can write the following surface-area fraction

$$\phi_{\text{valve}} = \frac{N_{\text{valve}} S_{\text{valve}}}{S_{\text{mLV}}}, \tag{10}$$

and we have

$$L_p = \phi_{\text{valve}} L_{p,\text{micro}}. \tag{11}$$

Similarly, the structural model of the valve opening can be extended to estimate the molecular permeability P_{lymph}. We consider the transport of a solute across the valve governed by both diffusion and advection. At the microscale, the local solute flux $J(x)$ (molar or mass rate) through the cross-section $A(x) = w(x)T$ is described by Fick's first law and the convective contribution:

$$J(x) = -DTw(x)\frac{dC}{dx} + (1-\sigma)Q_{\text{valve}}C(x), \tag{12}$$

where D is the diffusion coefficient of the solute in the lymph and σ is the reflection coefficient. For the open valve configuration where $w(x)$ is significantly larger than the solute's molecular radius, we assume $\sigma \approx 0$.

To obtain an explicit solution for the effective molecular permeability, we consider a steady-state concentration difference $\Delta C = C_i - C_L$, where C_i is the interstitial concentration and C_L is the concentration in the lymphatic lumen. Under the physiological assumption of a *sink condition* in the lymphatic vessels, where the solute is rapidly cleared by the flow, we set $C_L = 0$ and $\Delta C = C_i$.

The total solute flux passing through a single primary valve, J_{valve}, is the sum of the diffusive and advective components:

$$J_{\text{valve}} = J_{\text{diff}} + J_{\text{adv}} = \left(\frac{DT}{\int_0^{L_{\text{valve}}+\Delta L_{\text{valve}}} \frac{1}{w(x)} dx} \right) \Delta C + Q_{\text{valve}} \bar{C}, \tag{13}$$

where $\bar{C}$ is the average concentration of the solute in the trans-valve flow. Under the sink condition $C_L = 0$ and assuming the fluid enters the valve from the interstitium, we have $\bar{C} = C_i = \Delta C$.

We define the microscale effective molecular permeability as:

$$P_{\text{micro,eff}} = \frac{J_{\text{valve}}}{S_{\text{valve}}\Delta C} = P_{\text{micro,diff}} + \frac{Q_{\text{valve}}}{S_{\text{valve}}}, \tag{14}$$

where $P_{\text{micro,diff}}$ is the purely diffusive permeability obtained from the integral of the inverse gap height $1/w(x)$.

Finally, applying the same upscaling framework used for the hydraulic permeability, the macroscale effective molecular permeability P_{eff} of the lymphatic vessel wall is given by:

$$P_{\text{eff}} = \phi_{\text{valve}} P_{\text{micro,eff}}. \tag{15}$$

Substituting the surface-area fraction ϕ_{valve}, we obtain the final relation:

$$P_{\text{eff}} = \phi_{\text{valve}} P_{\text{micro,diff}} + \frac{Q_{\text{flux}}}{S_{\text{mLV}}}, \tag{16}$$

where Q_{flux} is the net volumetric drainage of the network. This formulation allows us to estimate the total solute clearance $F_{\text{solute}} = P_{\text{eff}} S_{\text{mLV}} C_i$ directly from the structural parameters of the Mendoza model.

A.1 QMC Analysis

The QMC simulation is based on 60 million samples. The validity of each parameter set was evaluated against a multi-objective cost function. The algorithm minimizes the cumulative relative error between the model outputs and two specific physiological targets:

1. **Net Lymphatic Flux (Q_{flux}):** The drainage capacity of the network. We set as target the production rate of $0.5\,\text{L/day} \approx 5.8 \times 10^{-9}\,\text{m}^3/\text{s}$ [3] against our computed total $Q_{\text{flux}} = -L_p S_{\text{mLV}} \Delta P_{\text{at}}$.

2. **Total Vascular Volume:** The volume occupied by the mLVs network; we test two targets: $V_{\text{mLV}} \approx 6 \times 10^{-6}\,\text{m}^3$ [4] and $V_{\text{mLV}} = 4.57 \times 10^{-7}\,\text{m}^3$ (see Section F) against our computed volume of $S_{\text{tot}} r/2$.

The sampled parameters and ranges are

$$\Delta P_{\text{at}} \in [-1750, -400]\ \text{Pa}, \quad L_p \in [10^{-12}, 10^{-8}]\ \text{m/Pa} \cdot \text{s},$$

$$r \in [5 \times 10^{-6}, 2 \times 10^{-5}]\ \text{m}, \quad L_{FIX} = L_{\text{valve}} + \Delta L_{\text{valve}} \in [5 \times 10^{-7}, 6 \times 10^{-6}]\ \text{m}.$$

For a porosity of 0.5%, the near-optimal subset (9,207 accepted samples) yields the following mean values, 95% confidence intervals, and coefficients of variation (CV):

$$\begin{aligned}
\Delta P_{\text{at}} &= -6.71 \times 10^2\ [-6.76 \times 10^2,\ -6.66 \times 10^2]\ \text{Pa}, \quad (\text{CV} = 37.0\%) \\
L_p &= 4.42 \times 10^{-10}\ [4.37 \times 10^{-10},\ 4.46 \times 10^{-10}]\ \text{m/Pa} \cdot \text{s}, \quad (\text{CV} = 48.5\%) \\
r &= 4.02 \times 10^{-5}\ [4.00 \times 10^{-5},\ 4.05 \times 10^{-5}]\ \text{m}, \quad (\text{CV} = 34.4\%) \\
L_{\text{FIX}} &= 6.11 \times 10^{-7}\ [6.09 \times 10^{-7},\ 6.13 \times 10^{-7}]\ \text{m}, \quad (\text{CV} = 13.2\%)
\end{aligned}$$

Using the confidence interval means, the derived total vessel surface area for the active network is $S_{\text{mLV}} \approx 1.95 \times 10^{-2}\ \text{m}^2$.

The global sensitivity analysis (Table A) evaluates both the linear (Pearson) and monotonic nonlinear (Spearman rank) correlations to the estimated flux across the entire valid parameter space. It indicates that the net flux shows near-zero marginal correlation to individual parameters under both metrics.

Within this accepted near-optimal subset, strong structural correlations emerge (Figure B). Hydraulic conductivity L_p shows strong positive correlation with both radius r (0.71) and transmural pressure ΔP_{at} (0.58), while transmural pressure also correlates positively with L_{FIX} (0.51).

Table A: Sensitivity Analysis (Global Correlations) - 0.5% Porosity

Parameter	**Pearson w/ $Q_{\mathbf{flux}}$**	**Spearman w/ $Q_{\mathbf{flux}}$**
ΔP_{at}	-0.0015	-0.0021
L_p	-0.0015	-0.0022
r	0.0007	0.0015
L_{FIX}	-0.0004	-0.0011

Conversely, for the case of 6.5% porosity, the near-optimal subset (727 accepted samples) yields the following adjusted mean values, confidence intervals, and CVs:

$$\Delta P_{\text{at}} = -6.78 \times 10^{2}\ [-6.97 \times 10^{2},\ -6.60 \times 10^{2}]\ \text{Pa}, \quad (\text{CV} = 37.1\%)$$

$$L_p = 3.28 \times 10^{-11}\ [3.16 \times 10^{-11},\ 3.40 \times 10^{-11}]\ \text{m/Pa} \cdot \text{s}, \quad (\text{CV} = 50.0\%)$$

$$r = 3.97 \times 10^{-5}\ [3.87 \times 10^{-5},\ 4.07 \times 10^{-5}]\ \text{m}, \quad (\text{CV} = 35.7\%)$$

$$L_{\text{FIX}} = 6.08 \times 10^{-7}\ [6.03 \times 10^{-7},\ 6.14 \times 10^{-7}]\ \text{m}, \quad (\text{CV} = 13.2\%)$$

Using these corresponding CI means, the derived total vessel surface area for the active network scales up to $S_{\text{mLV}} \approx 2.60 \times 10^{-1}\ \text{m}^2$.

The global sensitivity analysis for this higher porosity level (Figure B) evaluates the same metrics. Similar to the lower porosity case, it indicates that the net flux maintains a near-zero marginal correlation to individual parameters.

Table B: Sensitivity Analysis (Global Correlations) - 6.5% Porosity

Parameter	**Pearson w/ $Q_{\mathbf{flux}}$**	**Spearman w/ $Q_{\mathbf{flux}}$**
ΔP_{at}	-0.0018	-0.0035
L_p	-0.0004	-0.0004
r	0.0015	0.0029
L_{FIX}	-0.0017	-0.0023

Within this accepted near-optimal subset, strong structural correlations again emerge (Figure B). Consistent with the 0.5% porosity case, hydraulic conductivity L_p shows a strong positive correlation with both radius r (0.73) and transmural pressure ΔP_{at} (0.56), while transmural pressure continues to correlate with L_{FIX} (0.51).

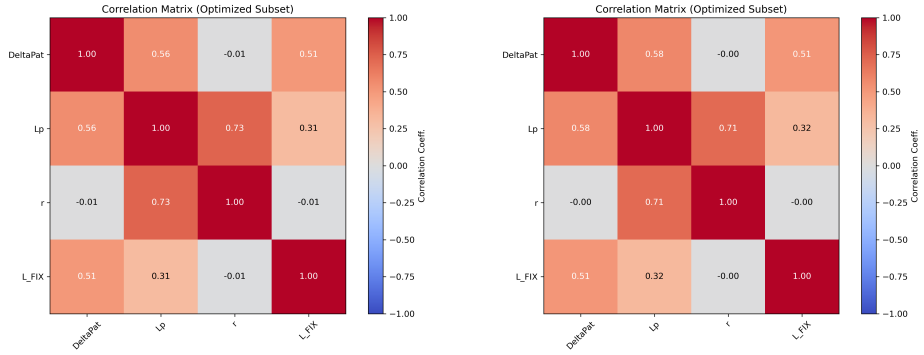

Fig. B: The correlation matrix of the near-optimal subset obtained from the Quasi-Monte Carlo simulation, illustrating the morphometric and mechanical trade-offs of the dural lymphatic network. **Left:** Case with porosity $\phi_L = 6.5\,\%$. **Right:** Case with porosity $\phi_L = 0.5\,\%$.

The global sensitivity analysis (Tables A and B) reveals that the Net Lymphatic Flux (Q_{flux}) exhibits near-zero marginal correlation to any individual parameter under both linear (Pearson) and rank-based (Spearman) metrics. This is due to the fact that ($Q_{\mathrm{flux}} \propto -L_p S_{\mathrm{mLV}} \Delta P_{\mathrm{at}}$), which means that the drainage capacity cannot be dictated by a single "bottleneck" variable but requires the simultaneous co-optimization of permeability (L_p), network surface area (S_{mLV}), and the transmural pressure gradient (ΔP_{at}). Notably, while L_p and S_{mLV} differ significantly depending on the tissue porosity, their product ($L_p S_{\mathrm{mLV}}$) remains consistent, emphasizing that the system fundamentally relies on the balance between permeability and available surface area to maintain adequate flux. The model successfully found an effective vessel average radius of $r \approx 39.7$ to $40.2\,\mu$m across the two porosity cases, which falls perfectly within the observed anatomical bounds for initial and collecting lymphatic vessels [5, 6].

Using the estimation above, we can compute the effective permeability of the lymphatic vessels as well using equation (16). We test the simulation with different ϕ_L and we notice that, as for the parameter L_p, what remains constant through different lymphatic permeabilities is the product $P_{\text{eff}} S_{\text{mLV}} = 5.79 \times 10^{-9}\,\text{m}^3/\text{s}$. For modeling purpose, we define the quantity $\beta = \dfrac{P_{\text{eff}} S_{\text{mLV}}}{V_{\text{dura}}} \approx 0.228\,1/\text{h}$. By employing our estimated $P_{\text{eff}} S_{\text{mLV}}$ and assuming a solute production rate of 3 g/day (equivalent to a flux of 0.0018 mmol/h), we obtain an interstitial concentration of approximately 0.0864 mmol/L. This estimate is exceptionally consistent with the concentration values derived from the gMRI segmentation reported in the main text.

B Parameters exploration in a Two Compartment ODE Model

We describe the tracer transport between the CSF compartment concentration $C_{CSF}(t)$ and the Dura compartment concentration in a simplified ODE model in the following way:

$$\frac{\mathrm{d}\phi_{\text{CSF}} C_{\text{CSF}}}{\mathrm{d}t} = -\alpha\,(C_{CSF} - C_D) - \bar{k}_{10}\, C_{\text{CSF}} + I(t), \tag{17}$$

$$\frac{\mathrm{d}\phi_D C_D}{\mathrm{d}t} = \alpha\,(C_{CSF} - C_D) - \bar{k}_D\, C_D, \tag{18}$$

where $C_{\text{CSF}}(t)$ and $C_D(t)$ are the concentrations in the whole CSF and dural compartments, respectively, α [h^{-1}] is the influx rate constant (mass transfer coefficient) from CSF to the dura, $\bar{k}_{10}$ [h^{-1}] is the total efflux or clearance rate constant from the CSF, $\bar{k}_D$ [h^{-1}] is the total efflux or clearance rate constant from the dura, $I(t)$ is the injection of gadobutrol in the CSF compartment (that needs to be modelize).

Initial conditions were set to $C_{\text{CSF}}(0) = C_D(0) = 0$.

Since we are not considering the space variable in this model, it is better to reformulate it in terms of amounts instead of concentrations

$$\frac{\mathrm{d}A_1}{\mathrm{d}t} = -\left(k_{12} + k_{10}\right) A_1 + k_{21} \frac{V_{\mathrm{CSF}}}{V_D} A_2 + I(t), \tag{19}$$

$$\frac{\mathrm{d}A_2}{\mathrm{d}t} = k_{12} \frac{V_D}{V_{\mathrm{CSF}}} A_1 - \left(k_{21} + k_D\right) A_2, \tag{20}$$

where A_1 and A_2 are the amounts (in mmol) of gadobutrol in the CSF and dura compartment, respectively;

$$k_{12} = \frac{\alpha}{\phi_{\mathrm{CSF}}}, \qquad k_{21} = \frac{\alpha}{\phi_{\mathrm{D}}},$$

$$k_{10} = \frac{\bar{k}_{10}}{\phi_{\mathrm{CSF}}}, \quad k_D = \frac{\bar{k}_D}{\phi_{\mathrm{D}}},$$

and the injection is modeled as the best fit between the following models

$$I(t) = S_{\mathrm{in}} t^{B_{\mathrm{in}}} \exp(-t/C_{\mathrm{in}}), \qquad I(t) = S_{\mathrm{in}} \left(\exp(-t/B_{\mathrm{in}}) - \exp(-t/C_{\mathrm{in}})\right).$$

B.1 QMC Analysis

The search space consisted of seven dimensions representing the unknown parameters of the model: k_{10} (elimination from the CSF), k_{12} (transfer from CSF to Dura), k_{21} (return from Dura to CSF), k_D (clearance), S_{in} (scaling factor), B_{in} (first decay constant), and C_{in} (second decay constant). To reduce the number of dimensions for this analysis, the parameters S_{in}, B_{in}, and C_{in} are fitted against the CSF concentration data and then we vary them of 10 % to decrease the uncertainity given by these parameters. Moreover, we apply an optimization method (L-BFGS-B) to the 90% confidence interval found by the Montecarlo simulations to obtain the parameters that best fit the results in that range. To evaluate the goodness-of-fit for each simulated trajectory against the experimental data, a Normalized Sum of Squared Residuals (SSR) was computed.

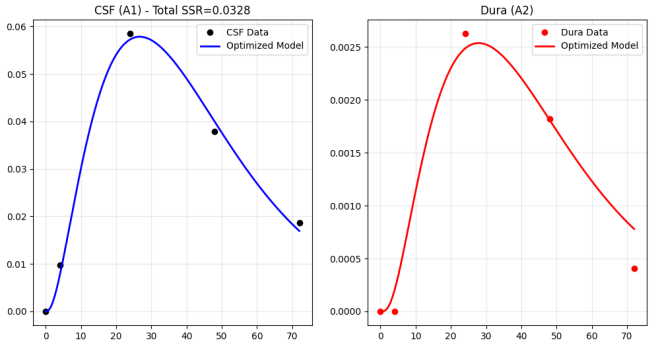

Fig. C: The best fit models of the two compartment (without the $4h$ data point)

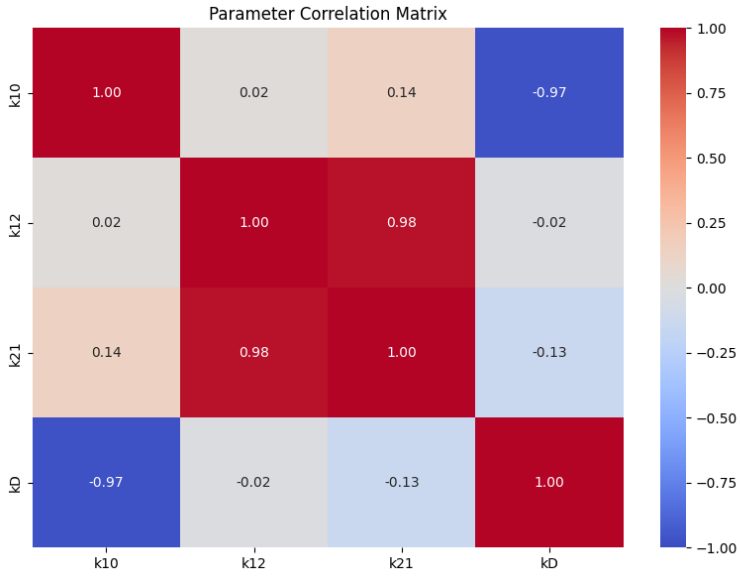

Fig. D: The correlation matrix of the 0D model.

The refined two-compartment model, successfully captured the macroscopic tissue kinetics with a final optimized Sum of Squared Residuals (SSR) of 0.0328 (see Figure C). Moreover, Figure D shows the correlation matrix between the parameters.

The QMC analysis of the model (19) – (20) provided a rigorous assessment of the practical identifiability of the physiological parameters. The statistical analysis revealed remarkably low Spearman sensitivities to the cost function across all parameters ($|\rho| < 0.05$). Consequently, the QMC 95% confidence intervals remained exceptionally broad for both the exchange rates (e.g., $k_{21} \in [0.0001, 77.03]$ h^{-1}) and the elimination pathways (e.g., $k_D \in [0.0002, 6.79]$ h^{-1}). However, this apparent lack of individual parameter identifiability is fundamentally explained by the presence of strong compensatory processes within the system, as evidenced by the Pearson correlation matrix. Specifically, we observed a near-perfect negative correlation between the two elimination pathways (k_{10} and k_D, $r \approx -0.97$), indicating that the model easily compensates for a lower direct CSF clearance by increasing dural clearance to maintain the overall systemic elimination rate. Similarly, a highly significant positive correlation was found between the compartment exchange rates (k_{12} and k_{21}, $r \approx 0.98$). While this strong coupling renders the exact individual magnitudes of k_{12} and k_{21} difficult to isolate independently, it carries critical physiological significance, but their ratio k_{12}/k_{21} is identifiable and it corresponds to the physiological parameter ratio $\eta = \phi_D/\phi_{\text{CSF}}$. Due to the broad parameter results range, $\eta \in [0.18, 244]$; removing the non-physiological values, we restrict the parameter interval at $\eta \in [0.18, 0.6]$.

C Parameter Exploration in a One-Dimensional One Compartment PDE Model

C.1 Model

The transport of the solute is modeled within a spherically symmetric, single-porosity domain representing the tissue layer.

The geometric domain is defined as a spherical shell bounded by an inner radius R_1 and an outer radius R_2. Assuming spherical symmetry, the concentration profile

$C(r,t)$ varies only with the radial distance $r \in [R_1, R_2]$ and time t. The values of R_1 and R_2 were found such that $R_2 - R_1 \approx 1\,\text{mm}$ (approximately the thickness of the dura [7]) and a volume of $V_D \approx 0.0914\,\text{L}$ (found by the segmentation presented in Section 2.2). With these constrains, we found $R_1 = 0.848\,\text{dm}$ and $R_2 = 0.858\,\text{dm}$.

The solute concentration $C(r,t)$ is governed by a one-dimensional radial reaction-diffusion equation. The model accounts for Fickian diffusion and a volumetric clearance (sink) term. The governing partial differential equation (PDE) is given by:

$$\frac{\partial C}{\partial t} = \nabla \cdot (D_D \nabla C) - \frac{K_D}{\phi} C; \tag{21}$$

expanded in spherical coordinates, this yields:

$$\frac{\partial C}{\partial t} = \frac{D_D}{r^2} \frac{\partial}{\partial r} \left(r^2 \frac{\partial C}{\partial r} \right) - \frac{K_D}{\phi} C, \tag{22}$$

where D_D is the effective diffusion coefficient (dm^2/h) that describes the diffusion and eventually the dispersion in the whole dura (including the venous and lymphatic vessels) and K_D is the clearance coefficient (h^{-1}).

Inner Boundary ($r = R_1$): Transport across the inner surface is dictated by a permeability coefficient P (dm/h). This is represented as a Robin (mixed) boundary condition where the diffusive flux matches the permeable flux driven by the concentration difference between the CSF driver $C_{\text{CSF}}(t)$ and the tissue surface $C(R_1, t)$:

$$-D_D \frac{\partial C}{\partial r}\bigg|_{r=R_1} = \frac{P}{\phi} \big(\eta C_{\text{CSF}}(t) - C(R_1, t) \big), \tag{23}$$

where $\eta = \phi_D / \phi_{\text{CSF}}$. The CSF input function $C_{\text{CSF}}(t)$ is defined empirically using best fit between the following models

$$I(t) = S_{\text{in}} t^{B_{\text{in}}} \exp(-t/C_{\text{in}}), \qquad C_{\text{CSF}}(t) = S_{\text{in}} \left(\exp(-t/B_{\text{in}}) - \exp(-t/C_{\text{in}}) \right),$$

where S_{in}, B_{in}, and C_{in} are fixed parameters derived from prior curve fitting.

Outer Boundary ($r = R_2$): The outer boundary is assumed to be strictly impermeable, yielding a homogeneous Neumann (no-flux) boundary condition:

$$\left.\frac{\partial C}{\partial r}\right|_{r=R_2} = 0. \tag{24}$$

Initial Condition ($t = 0$): The tissue is assumed to be initially free of the solute, yielding:

$$C(r, 0) = 0 \quad \text{for} \quad R_1 \leq r \leq R_2 \tag{25}$$

To compare the continuous spatial model against bulk empirical data, the observable concentration is defined as the volume-weighted average of $C(r, t)$ across the entire spherical shell:

$$\bar{C}(t) = \frac{1}{V_{\text{total}}} \int_{R_1}^{R_2} C(r, t) \cdot 4\pi r^2 \, dr \tag{26}$$

where $V_{\text{total}} = \frac{4}{3}\pi(R_2^3 - R_1^3)$ is the total volume of the domain. This $\bar{C}(t)$ is subsequently used to compute the objective function (Normalized Root Mean Square Error) during the parameter optimization process. We run QMC to estimate parameters 95 % confidence intervals. We can see the results in Table C.

C.2 QMC analysis and Results

We rely on the QMC method with Halton sequence to estimate the parameters D_D, K_D/ϕ, and P/ϕ. We choose as parameter range the following (motivated by biology and range found in the 0D model of Section B): $D_D \in [1 \times 10^{-5}, 5 \times 10^{-3}]\,\text{dm}^2/\text{h}$ [8–10], $P/\phi \in [10^{-4}, 100]\,\text{dm/h}$, $K_D/\phi \in [10^{-4}, 100]\,1/\text{h}$, and $\eta \in [0.18, 0.6]$.

To ensure a comprehensive and physiologically relevant exploration of the 1D diffusion-reaction model, the parameter search space was constrained using insights from the prior 0D compartmental analysis. Specifically, the search boundaries for the

effective clearance rate (K_D/ϕ) and the effective boundary permeability (P/ϕ) were informed directly by the confidence intervals of their macroscopic analogs derived from the 0D model. Conversely, the limit for the internal diffusion coefficient (D_D) was set broad enough to allow the numerical solver to freely explore both extreme diffusion-limited and permeability-limited (well-mixed) transport regimes, but the extrema were set inspired by biological limit [9–11].

The optimal parameter set for the 1D diffusion-reaction model yielded a minimum Sum of Squared Residuals (SSR) of approximately 0.068. To assess the structural identifiability and robustness of these estimates, a subset analysis was performed on the top 250 model fits. The statistical summary of the physical and derived parameters is presented in Table C.

Table C: Statistical Summary of Estimated Parameters (Top 250 Fits). CV denotes the Coefficient of Variation ($SD/Mean$), serving as a metric for parameter identifiability.

Parameter	Symbol	Mean	Std. Dev.	Median	Rel. IQR	CV (%)
Permeability (dm/h)	P/ϕ	0.0040	0.0015	0.0039	0.703	38.6%
Partition Coeff. (-)	η	0.3186	0.1290	0.2800	0.751	40.5%
Clearance Rate (h^{-1})	K_D/ϕ	0.2129	0.1363	0.2175	1.173	64.1%
Diffusion Coeff. (dm^2/h)	D_D	1.14×10^{-3}	1.26×10^{-3}	5.29×10^{-4}	3.025	110.8%

Table D: Statistical Summary of Estimated Parameters (Top 250 Fits). CV denotes the Coefficient of Variation ($SD/Mean$). Results refer to the single-compartment model with fixed $\eta = 0.3186$.

Parameter	Symbol	Mean	Std. Dev.	Median	Rel. IQR	CV (%)
Clearance Rate (h^{-1})	K_D/ϕ	0.2466	0.0169	0.2463	0.108	6.8%
Permeability (dm/h)	P/ϕ	0.0037	0.0003	0.0037	0.133	9.4%
Diffusion Coeff. (dm^2/h)	D_D	1.16×10^{-3}	1.29×10^{-3}	6.03×10^{-4}	2.617	110.7%

The correlation matrix of Figure E reveals high correlation between the parameters P, η, and K_D. The correlation between P and eta is given by the product $P\eta$ at the

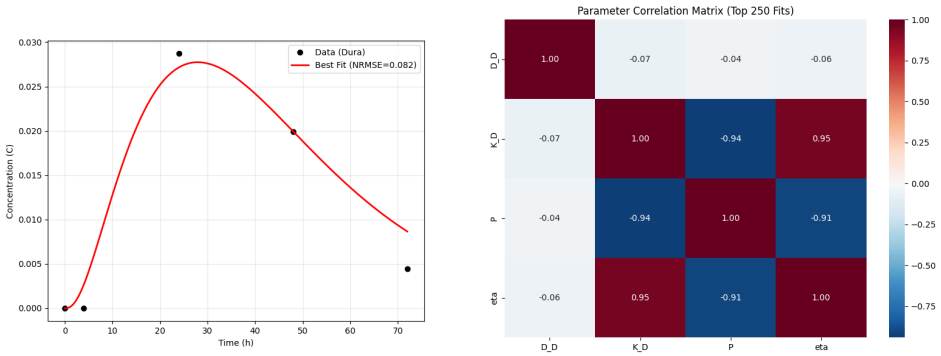

Fig. E: **Left**: The best fit models of the 1 compartment model on a sphere. **Right**: The correlation matrix of the spherical 1 compartment model.

boundary condition. By fixing the partition coefficient at its mean value ($\eta = 0.3186$), we successfully decoupled the boundary dynamics, yielding high identifiability for the clearance rate (K_D) and permeability (P), which exhibit low Coefficients of Variation (6.8% and 9.4%, respectively, see Table D). This stability confirms that the previously observed uncertainties were primarily numerical artifacts of the P-η correlation.

The parameter correlation matrix highlights a strong positive coupling between K_D and P ($r = 0.738$). This relationship elucidates a fundamental physiological trade-off: higher dural permeability, which increases tracer influx, must be balanced by a proportionally higher clearance rate to accurately replicate the washout decay observed in clinical data. This compensatory mechanism ensures that the model preserves the mass balance and the observed peak timing, regardless of the individual parameter magnitudes.

The internal diffusion estimation $D_D \approx 1.16 \times 10^{-3}$ dm^2/h presents high uncertainty (CV $> 100\%$), but it offers a value higher than the gadobutrol diffusion in free water of $\approx 1.37 \times 10^{-4}$ dm^2/h, suggesting that the only-diffusion regime is not enough.

D Parameter Exploration in a One-Dimensional Two Compartment PDE Model

D.1 Model

The transport of the solute is modeled within a spherically symmetric, double-porosity domain representing the tissue layer. The geometric domain is defined as a spherical shell bounded by an inner radius R_1 and an outer radius R_2.

To account for the complex microstructure of the tissue, the continuum is divided into two distinct, overlapping interacting compartments: the Dura (D) and the Lymph (L). The concentration profiles for both compartments, $C_D(r,t)$ and $C_L(r,t)$, vary with the radial distance $r \in [R_1, R_2]$ and time t.

In this model, we suppose that the entire clearance from the dura is given by the mLVs direct towards the cervical lymphatic vessels. We suppose this to test if it is possible to have a full clearance given by the lymphatics and to estimate the parameters which make this possible.

The spatio-temporal evolution of the solute is governed by a coupled system of one-dimensional radial reaction-diffusion equations.

For the primary tissue compartment (Dura, C_D), transport is driven by Fickian diffusion and mass exchange with the secondary compartment:

$$\frac{\partial C_D}{\partial t} = \frac{D_D}{r^2}\frac{\partial}{\partial r}\left(r^2 \frac{\partial C_D}{\partial r}\right) + \beta(\phi_R C_L - C_D), \tag{27}$$

For the secondary compartment (Lymph, C_L), transport involves diffusion, the reverse mass exchange, and a volumetric clearance (elimination) term:

$$\frac{\partial C_L}{\partial t} = \frac{D_L}{r^2}\frac{\partial}{\partial r}\left(r^2 \frac{\partial C_L}{\partial r}\right) - \beta(\phi_R C_L - C_D) - k_{\text{elim}} C_L \tag{28}$$

where D_D and D_L are the effective diffusion coefficients for the Dura and Lymph compartments, respectively (dm^2/h), $\beta = \bar{\beta}/\phi_D$ is the exchange rate between the two

compartments (h^{-1}), $\phi_R = \phi_D/\phi_L$, $\phi = \phi_D + \phi_L$ and ϕ_D takes into consideration the porosity of the dura matrix and the venous vessels inside the dura, and $k_{\text{elim}} = \bar{k}_{\text{elim}}/\phi_L$ is the lymphatic clearance coefficient given by cervical lymphatic vessels (h^{-1}).

Inner Boundary ($r = R_1$): Transport from the CSF into the Dura compartment is dictated by a permeability coefficient $P = \bar{P}/\phi_D$ (dm/h). A scaling factor $\eta_D = \phi_D/\phi_{\text{CSF}}$ is applied to the CSF driving function. The Lymph compartment is assumed to have no direct exchange with the CSF at this boundary.

$$-D_D \frac{\partial C_D}{\partial r}\bigg|_{r=R_1} = P\big(\eta C_{\text{CSF}}(t) - C_D(R_1, t)\big), \tag{29}$$

$$-D_L \frac{\partial C_L}{\partial r}\bigg|_{r=R_1} = 0. \tag{30}$$

The CSF input function $C_{\text{CSF}}(t)$ is defined empirically using a bi-exponential model:

$$C_{\text{CSF}}(t) = St^{Bt}e^{-t/C_{\text{rate}}} \tag{31}$$

where S, B, and C_{rate} are fixed parameters derived from prior data fitting.

Outer Boundary ($r = R_2$): The outer boundary is assumed to be strictly impermeable for both compartments, yielding homogeneous Neumann (no-flux) boundary conditions:

$$\frac{\partial C_D}{\partial r}\bigg|_{r=R_2} = 0, \quad \frac{\partial C_L}{\partial r}\bigg|_{r=R_2} = 0 \tag{32}$$

Initial Condition ($t = 0$): Both compartments are assumed to be initially free of the solute:

$$C_D(r,0) = 0 \quad \text{and} \quad C_L(r,0) = 0 \quad \text{for} \quad R_1 \leq r \leq R_2 \tag{33}$$

To evaluate the mathematical model against bulk tissue empirical data, the observable concentration is defined as the sum of the volume-weighted averages of both compartments across the entire spherical shell:

$$\bar{C}_{\text{Total}}(t) = \frac{1}{V_{\text{total}}} \int_{R_1}^{R_2} \big(C_D(r,t) + C_L(r,t)\big) \cdot 4\pi r^2 \, dr \tag{34}$$

where $V_{\text{total}} = \frac{4}{3}\pi(R_2^3 - R_1^3)$ is the total volume of the domain. This aggregate $\bar{C}_{\text{Total}}(t)$ is utilized to compute the objective function (Normalized Root Mean Square Error) during Montecarlo simulations. We run QMC to estimate parameters 95 % confidence intervals. We can see the results in Table **??** and the details about the QMC sampling in Supplementary D.

D.2 QMC Analysis

The search space consisted of six dimensions representing the unknown parameters of the model: the diffusion coefficient of the dura phase D_D (dm^2/h), the dura-lymphatc exchange β/ϕ_D (1/h), the porosity ratio ϕ_R, the diffusion coefficient of the lymph phase D_L (dm^2/h), the volumetric sink k_{elim}/ϕ_L (1/h), and the permeability between the dura and the CSF P/ϕ_D (dm/h). To have a parameter range that takes into account the 1 dimensional 1 compartment model, the following relationship are considered. First, we have that $\frac{k_{\text{elim}}}{\phi_L} = \frac{K_D}{\phi}(\phi_R + 1)$.

For the diffusion coefficients D_D and D_L, from the fact that the 1-compartment diffusion coefficient $D_D^{1comp} = \frac{\phi_D + \phi_L\gamma_L}{\phi_D + \phi_L} D$ where γ_L represents the enhancement diffusion given by the convection in the lymphatics, we use the following relationship: $D_L = D_D^{1comp}(\phi_R + 1) - \phi_R D_D$, where $D_D \in [2 \times 10^{-5}, 5 \times 10^{-5}]\,\text{dm}^2/h$ adapted from [12]; $\frac{k_{\text{elim}}}{\phi_L} \in [0.1(\phi_R + 1), 1(\phi_R + 1)]$, $\phi_R = \phi_D/\phi_L$ supposing a bound for ϕ_D similar to the gray matter ($\approx 0.1 - 0.3$) and for $\phi_L \in [0.005, 0.07]$, $\phi_R \in [2, 60]$, from

the (wider) 1-compartment model we have $P/\phi \in [0.001, 0.1]$, in our case we need $\frac{P}{\phi_D} = \frac{P}{\phi}\left(1 + \frac{1}{\phi_R}\right)$, the $\eta_D = \frac{\phi_D}{\phi_{\text{CSF}}} = \eta\left(\frac{\phi_R}{\phi_R+1}\right)$ where $\eta = \frac{\phi_D}{\phi_{\text{CSF}}}$ is given in the 1-compartment model as $\eta = 0.31$, and $\beta/\phi_D \in [0.5, 3]$ from Supplementary A and the range for ϕ_D.

The optimal parameter set for this double-porosity model yielded a minimum Sum of Squared Residuals (SSR) of approximately 0.082. To assess structural identifiability and the robustness of these constrained estimates, a subset analysis was performed on the top 250 model fits (the upper 5% convergence region). The statistical summary of the macroscopic and derived parameters is presented in Table E.

The estimated lymphatic diffusion coefficient ($D_L \approx 1.69 \times 10^{-2}$ dm^2/h) is approximately two orders of magnitude higher than the established free-water diffusion coefficient of Gadobutrol (1.37×10^{-4} dm^2/h). Such an unphysiologically high diffusivity suggests that the QMC algorithm is mathematically forcing the diffusion term to compensate for macroscopic advective transport, which is inherently absent from the current governing equations. This phenomenon strongly indicates that a pure diffusion model is insufficient to fully capture the complex, rapid transport dynamics within the dural lymphatic and vascular networks, pointing to advection-driven flow as a critical mechanism that must be accounted for to accurately describe dural clearance.

To further validate whether this behavior was an artifact of boundary conditions, we tested the model using a different partition coefficient ($\eta = 0.18$). As anticipated from the parameter coupling observed in the single-compartment analysis presented in Supplementary C, modifying η induced expected proportional shifts in the boundary permeability (P) and elimination (k_{elim}) parameters to preserve the overall mass balance. Crucially, however, the artificially high magnitude of D_L remained consistent. This persistence confirms that the inflated D_L is not a numerical artifact driven by boundary correlations, but rather a fundamental structural limitation.

Table E: Statistical Summary of Estimated Parameters for the 2-Compartment Model (Top 250 Fits). CV denotes the Coefficient of Variation ($SD/Mean$), serving as a metric for parameter identifiability.

Parameter	Symbol	Mean	Std. Dev.	Median	Rel. IQR	CV (%)
Permeability (dm/h)	P	0.0045	0.0003	0.0045	0.057	6.1%
Primary Diffusion (dm^2/h)	D_D	4.50×10^{-5}	3.00×10^{-6}	4.60×10^{-5}	0.105	7.7%
Exchange Rate (h^{-1})	β	2.25	0.51	2.29	0.334	22.6%
Lymphatic Diffusion (dm^2/h)	D_L	1.69×10^{-2}	7.87×10^{-3}	1.76×10^{-2}	0.752	46.6%
Elimination Rate (h^{-1})	k_{elim}	9.51	4.48	10.01	0.733	47.1%
Porosity Ratio (-)	ϕ	33.79	16.24	35.37	0.764	48.1%

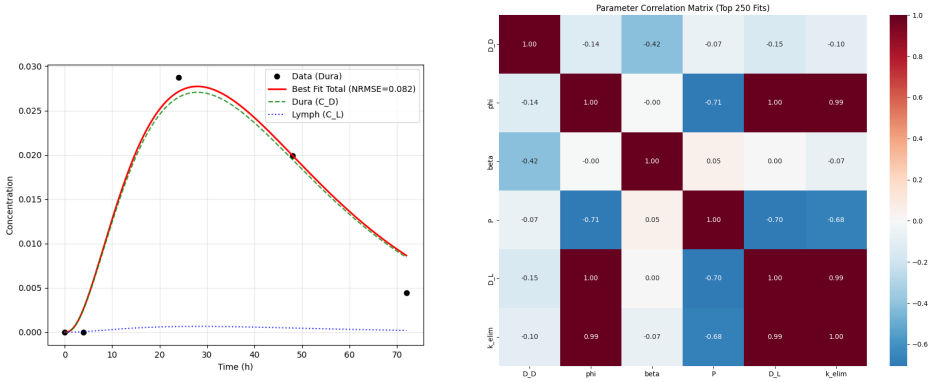

Fig. F: **Left**: The best fit models of the 2 compartment model on a sphere. **Right**: The correlation matrix of the spherical 2 compartment model.

E Dura and Lymphatic Permeabilities

Using the explicit formula for the permeability $K = \dfrac{Q\Delta x}{A\Delta p}$, we have that that $A = V/\Delta x$, using the $V = 9.489 \times 10^{-5}\,\mathrm{m}^2$ and $\Delta x = 0.001\,\mathrm{m}$, assuming a flux of $Q = 0.5\,\mathrm{L/day} \approx 5.8 \times 10^{-9}\,\mathrm{m}^3/\mathrm{s}$, we have the relationship

$$K_D = \mu K = \frac{4.28 \times 10^{-14}}{\Delta P}.$$

Using the data estimated in Supplementary A, we have an estimated permeability value of $K_D \approx 5.2 \times 10^{-17}\,\mathrm{m}^2$.

Using the same approach, we can estimate the permeability of the mLVs as well. For the mLVs we need to consider that the flow goes in the "polar" direction, hence we have that as characteristic length we use an average value of $L \approx 10\,\text{cm}$; Moreover, we assume that the pressure at the upper part of the brain is $\approx 1.4 \times 10^3\,\text{Pa}$ [13] and is $0\,\text{Pa}$ in the exit region of the brain (cervical lymphatic vessels) [14, 15]; these lead to a permeability of $K_L \approx 2.39 \times 10^{-13}\,\text{m}^2$, smaller of one order of magnitude to the one found using an homogenization modeling approach in dermal lymphatic capillaries in [16].

F mLV Volume

We assume that the meningeal lymphatic vessels absorb all the fluid produced by the brain over one day ($Q_{\text{prod}} \approx 0.5\,\text{L/day} \approx 5.79 \times 10^{-9}\,\text{m}^3/\text{s}$). Furthermore, the average velocity in the basal mLVs is $\bar{v} \approx 2.2 - 2.7\,\text{mm/s}$ [17]. Using these data and assuming a spherical brain, we can estimate the porosity of the mLVs to be

$$\phi_L \approx \frac{Q_{\text{prod}}}{\bar{v} A_\perp} \approx 0.005 - 0.015 = 0.5\% - 1.5\,\%.$$

This value is lower respect to the porosity found of the dermal lymphatic vessels [16] ($\approx 5 - 20\,\%$). It follows that the mLVs volume is $V_{\text{mLV}} \approx 4.57 \times 10^{-7} - 1.37 \times 10^{-6}\,\text{m}^3$. Assuming a spherical shell geometry for the dura, the cross-sectional area $A_\perp$ perpendicular to the polar lymph flow is given by $A_\perp = V_{\text{dura}}/L$, where L represents the characteristic path length of the mLV (in polar direction, way through the cervical lymphatic vessels), and V_{dura} is the total volume.

In [4] they measured the volume of the meningeal lymphatic vessels and the venous vessels inside the dura. We have that the average volume of the mLV is $V_{\text{mLV}} \approx 6 \times 10^{-6}\ \text{m}^3$, which means a porosity of the mLV of $\phi_L \approx 0.063$. In [4] they did not measure the volume of the smaller mLVs found in [5], that represents a very small

fraction of the mLVs. Hence we can estimate that the porosity of the mLVs to be between $0.065 - 0.07$. Due to the uncertainity of these values, in this work we will consider a range for the porosity of the mLVs between $0.5 - 7\,\%$.

G Structural Identifiability and the Role of Local Dural Clearance (k_D)

To evaluate the impact of alternative drainage pathways, an extended formulation of the model was tested, incorporating a non-specific dural clearance parameter (k_D) adding the term $-\frac{k_D}{\phi_D} C_{D,i}$ to equation (2) of the main text. This parameter simulates the local reabsorption of the tracer in the dura mater without entering the lymphatic system, thereby acting in competition with the macroscopic lymphatic drainage towards the deep cervical lymph nodes (P_{DcLV}).

The Quasi-Monte Carlo (QMC) simulations of the extended model yielded an excellent experimental fit, with an optimal loss function (SSR = 0.055) identical to that of the base model presented in the main text. The ensemble statistics for this competitive scenario are detailed in Table F.

Table F: Optimal parameters and derived quantities (Top 200 QMC ensemble) for the extended model including local dural clearance (k_D).

Parameter	**Unit**	**Median**	**IQR [25%, 75%]**	**95% CI**
Model Parameters				
Partition Coeff. (ϕ)	[-]	7.69	[3.74, 14.57]	[2.26, 33.58]
CSF Permeability (P_{bot})	[h^{-1}]	0.434	[0.351, 0.557]	[0.239, 0.829]
Dispersion Coeff. (D_L)	[-]	0.0006	[0.0001, 0.0020]	[0.00001, 0.0043]
Deep Clearance (P_{DcLV})	[h^{-1}]	5.84	[0.085, 22.65]	[0.001, 231.54]
Dural Clearance (k_D)	[h^{-1}]	1.04	[0.086, 1.55]	[0.0002, 2.24]
Lymphatic Porosity (ϕ_L)	[-]	0.026	[0.013, 0.042]	[0.006, 0.066]
Derived Quantities				
Péclet Number (Pe)	[-]	54.22	[16.52, 513.74]	[2.92, 15855.82]
Biot Number (Bi)	[-]	177.21	[143.23, 227.44]	[70.28, 458.45]
Advection Time (T_{adv})	[h]	59.09	[28.95, 94.69]	[11.75, 154.43]
Diffusion Time (T_{diff})	[h]	3419.89	[999.64, 23042.68]	[430.72, 201782.79]

G.1 Discussion of Results and Equifinality

The inclusion of k_D significantly alters the hydrodynamic balance of the system. By allowing the dura mater to act as a local clearance pathway (with an estimated half-life of approximately 6.3 hours, $k_D \approx 0.11$ h^{-1}), the burden on the lymphatic system is drastically reduced. Consequently, the model predicts a slower advection time ($T_{adv} \approx$ 46.7 h) and a markedly reduced basal clearance P_{DcLV}. Nevertheless, the transport regime within the lymphatic vessels remains undeniably dominated by convection, as confirmed by a median Péclet number firmly greater than unity ($Pe \approx 54.22$).

Despite the physiological plausibility of this extended scenario, the simultaneous inclusion of k_D and P_{DcLV} introduces a well-known mathematical issue of *structural identifiability* (equifinality). Because contrast-enhanced MRI captures the global signal decay within a voxel but lacks the resolution to differentiate the specific molecular exit route or distinguish between interstitial or lymphatic enrishment, the QMC analysis can seamlessly compensate for an increase in one clearance parameter by decreasing the other, without altering the Sum of Squared Residuals (SSR).

G.2 Justification for the Base Model

In light of this, the model imposing $k_D = 0$ was adopted for the main text. Through this choice, the meningeal lymphatic network is forced to handle 100% of the tracer clearance.

This approach allows us to test the theoretical maximum capacity of the lymphatic network under a "worst-case scenario" approach. The results presented in the main text demonstrate that, even under this extreme load, the lymphatic system is physically capable of clearing the entire tracer volume using geometrically, physiologically, and anatomically realistic parameters. Therefore, the base model provides robust, independent computational validation of the clinical hypothesis that the meningeal

lymphatic network possesses sufficient hydraulic capacity to be the primary driver of brain clearance.

Data Avaiability

All the code and setup used in this supplementary material is avaiable upon request.

References

[1] Mendoza, E., Schmid-Schönbein, G.W.: A model for mechanics of primary lymphatic valves. Journal of Biomechanical Engineering **125**(3), 407–414 (2003) https://doi.org/10.1115/1.1568128

[2] Koch, T., Vinje, V., Mardal, K.: Estimates of the permeability of extra-cellular pathways through the astrocyte endfoot sheath. Fluids and Barriers of the CNS **20**(20) (2023) https://doi.org/10.1186/s12987-023-00421-8

[3] Pardridge, W.M.: Csf, blood-brain barrier, and brain drug delivery. Expert Opin Drug Deliv **13**(7), 963–975 (2016) https://doi.org/10.1517/17425247.2016.1171315

[4] Jacob, L., Brito Neto, J., Lenck, S., Corcy, C., Benbelkacem, F., Geraldo, L.H., Xu, Y., Thomas, J.M., El Kamouh, M.R., Spajer, M., Potier, M.C., Haik, S., Kalamarides, M., Stankoff, B., Lehericy, S., Eichmann, A., Thomas, J.L.: Conserved meningeal lymphatic drainage circuits in mice and humans. The Journal of experimental medicine **219** (2022) https://doi.org/10.1084/jem.20220891

[5] Vera Quesada, C.L., Rao, S.B., Torp, R., Eide, P.K.: Widespread distribution of lymphatic vessels in human dura mater remote from sinus veins. Frontiers in Cell and Developmental Biology **Volume 11 - 2023** (2023) https://doi.org/10.3389/fcell.2023.1228344

[6] Çavdar, S., Köse, B., Altınöz, D., Söyler, G., Cingöz, A., Gürses, .I.A., Özkan, M., Aşılyüksek, H., Çakır, H.: Lymphatic vessels accompanying dorsal and basal dural sinuses in the human brain. Journal of Chemical Neuroanatomy **134**, 102357 (2023) https://doi.org/10.1016/j.jchemneu.2023.102357

[7] Protasoni, M., Sangiorgi, S., Cividini, A., Culuvaris, G.T., Tomei, G., Dell'Orbo, C., Raspanti, M., Balbi, S., Reguzzoni, M.: The collagenic architecture of human dura mater. J Neurosurg **114**, 1723–1730 (2011) https://doi.org/10.3171/2010.12.JNS101732

[8] Riseth, J.N., Koch, T., Lian, S.L., Holck Storås, T., Zikatanov, L.T., Valnes, L.M., Nordengen, K., Mardal, K.-A.: Human brain MRI data of intrathecally injected tracer evolution over 72 hours for data-integrated simulations. Scientific Data (2026)

[9] Riseth, J.N., Koch, T., Mardal, K.-A.: Two-compartment modeling of tracer transport in the brain. In: Dokken, J.S., Mardal, K.-A., Rognes, M.E., Valnes, L.M., Vinje, V. (eds.) Mathematical Modelling of the Human Brain II: From Glymphatics to Deep Learning, pp. 105–122. Springer, ??? (2025)

[10] Hornkjøl, M., Valnes, L.M., Dokken, J.S.: Segmenting, meshing, and modeling CSF spaces. In: Dokken, J.S., Mardal, K.-A., Rognes, M.E., Valnes, L.M., Vinje, V. (eds.) Mathematical Modelling of the Human Brain II: From Glymphatics to Deep Learning. Simula SpringerBriefs on Computing, vol. 18, pp. 35–46. Springer, Cham (2026). https://doi.org/10.1007/978-3-032-00679-0_3

[11] Riseth, J., Koch, T., Lian, S., Storås, T., Zikatanov, L.T., Valnes, L.M., Nordengen, K., Mardal, K.-A.: The Gonzo Dataset: Human Brain MRI Data of CSF Tracer Evolution Over 72h For Data-Integrated Simulations. https://doi.org/10.5281/zenodo.14266867 . https://doi.org/10.5281/zenodo.14266867

[12] Bashkatov, A.N., Genina, E.A., Sinichkin, Y.P., Kochubey, V.I., Lakodina, N.A., Tuchin, V.V.: Glucose and mannitol diffusion in human dura mater. Biophysical Journal **85**(5), 3310–3318 (2003) https://doi.org/10.1016/S0006-3495(03)74750-X

[13] Vinje, V., Eklund, A., Mardal, K., Rognes, M., Støverud, K.: Intracranial pressure elevation alters csf clearance pathways. Fluids and Barriers of the CNS **17** (2020) https://doi.org/10.1186/s12987-020-00189-1

[14] Kim, D., Tithof, J.: Lumped parameter simulations of cervical lymphatic vessels: dynamics of murine cerebrospinal fluid efflux from the skull. Fluids and Barriers of the CNS **21** (2024) https://doi.org/10.1186/s12987-024-00605-w

[15] Kim, D., Tithof, J.: Fluid-structure interaction dynamics of cervical lymphatic vessel pumping and valvular function. bioRxiv (2025) https://doi.org/10.1101/2025.11.21.689846 https://www.biorxiv.org/content/early/2025/11/25/2025.11.21.689846.full.pdf

[16] Roose, T., Swartz, M.A.: Multiscale modeling of lymphatic drainage from tissues using homogenization theory. Journal of Biomechanics **45**(1), 107–115 (2012) https://doi.org/10.1016/j.jbiomech.2011.09.015

[17] Kim, J., Yoo, R., Choi, S.H., Park, S.: Non-invasive flow mapping of parasagittal meningeal lymphatics using 2d interslice flow saturation MRI. Fluids and Barriers of the CNS **20** (2023) https://doi.org/10.1186/s12987-023-00446-z